nature biomedical engineering

Article

https://doi.org/10.1038/s41551-025-01579-2

Wireless and bioresorbable triboelectric nerve block system for postoperative pain control

Received: 12 November 2024

Accepted: 29 October 2025

Young-Jun Kim[1,2,9], So-Hee Kim[1,3,9], Byung-Joon Park[1,3,9], Jinyoung Jeon[1,3], Donghyeon Kang[1,3], Youngwook Chung[2,4], Joon-Ha Hwang[2,4], Hong-Joon Yoon[5], Kyu Hyoung Lee[3] ✉, Byung-Ok Choi[6,7,8] ✉ & Sang-Woo Kim[1,3] ✉

Amidst the chronic issue of opioid misuse, finding an alternative to pharmaceutical pain control following surgical interventions stands as a major hurdle. Conventional non-pharmacological pain control technologies often rely on rigid stimulators linking internal and external body components, thereby imposing nerve burden and additional interventions for the removal. Here we introduce a bioresorbable triboelectric nerve cuff activated via ultrasounds for pain control. The targeted nerves are enveloped around polymers with opposite triboelectric properties that vibrate upon ultrasound stimulation, generating an alternating triboelectric field parallel to the nerve for pain modulation. In vivo testing in rat and porcine models demonstrates that the fully implanted neurostimulator exerts no discernible impact on gait and yields immediate pain relief. Application of the implant until full resorbing caused no adverse effects in the nerve or surrounding muscle tissue, and behavioural analysis confirmed its effective pain control. The implantable pain control system might offer a drug-free alternative to pain management strategies, helping prevent drug abuse.

Acute pain typically manifests suddenly and is often attributed to tissue damage resulting from injury, surgery or medical procedures. While serving as a vital warning signal to the body, acute pain can also introduce risks and complications if not effectively managed. While medications are commonly used for managing acute postoperative pain to ensure patient comfort and facilitate recovery, they entail considerable disadvantages. Notably, the use of opioid analgesics, prevalent for managing moderate to severe pain, presents concerns owing to potential side effects and the associated risks of addiction and dependence, particularly concerning long-term usage post-surgery[1,2]. Alternative approaches encompassing physical, electrical, optical and acoustic stimulation have been explored to address the inherent limitations of pharmacological pain control[3–10].

Among these, electrical stimulation of peripheral nerves is particularly attractive owing to its ability to modulate pain signalling in a targeted, reversible and nonaddictive manner. The efficacy of such

---

[1]Center for Human-oriented Triboelectric Energy Harvesting, Yonsei University, Seoul, Republic of Korea. [2]School of Advanced Materials Science and Engineering, Sungkyunkwan University, Suwon, Republic of Korea. [3]Department of Materials Science and Engineering, Yonsei University, Seoul, Republic of Korea. [4]Research and Development Center, Energymining, Suwon, Republic of Korea. [5]Department of Electronic Engineering, Gachon University, Seongnam-si, Republic of Korea. [6]Department of Neurology, Samsung Medical Center, Sungkyunkwan University School of Medicine, Seoul, Republic of Korea. [7]Cell and Gene Therapy Institute, Samsung Medical Center, Seoul, Republic of Korea. [8]Department of Health Science and Technology, Samsung Advanced Institute for Health Sciences and Technology, Seoul, Republic of Korea. [9]These authors contributed equally: Young-Jun Kim, So-Hee Kim, Byung-Joon Park. ✉e-mail: khlee2018@yonsei.ac.kr; bochoi@skku.edu; kimsw1@yonsei.ac.kr

stimulation depends less on the operating frequency and more on the physical proximity and invasiveness of the electrode relative to the nerve. Transcutaneous electrical nerve stimulation[11,12] applies current through skin patches and is completely non-invasive, but suffers from limited depth and targeting precision. Percutaneous electrical nerve stimulation[13], which uses temporary needle electrodes inserted near the nerve, enables both low- and high-frequency stimulation and is widely used in clinical pain trials. While percutaneous electrical nerve stimulation is widely used in clinical practice, its externalized configuration and limited spatial specificity restrict its application in fully implantable or precisely targeted nerve modulation systems. Cuff electrodes, typically used in kilohertz-frequency alternating current (KHFAC) approaches[3,5,14,15], directly surround the nerve and provide the most precise and effective method for nerve signal blocking. Therefore, KHFAC, which is directly connected to the nerve and blocks signals, has an excellent signal blocking effect, but it comes with several following disadvantages: (1) absence of energy source to be transferred through skin, (2) stiff and bulky components and (3) burden on the patient for the removal surgery. These limitations represent a technical barrier to the clinical use of electrical stimulation for non-pharmacological pain management, ultimately hindering their practical application in medical settings.

Herein we introduce an immediate pain control method with electrode-free and bioresorbable polymer using alternating triboelectric potential generated by the ultrasound. To achieve wireless electric field generation, we used an ultrasound-activated triboelectricity[16–18] that induces localized electrical modulation around the nerve. The nerve block system by alternating triboelectric-potential (NBAT), which has excellent biocompatibility and is made of a single polymer material with mechanical properties similar to nerves, does not cause any side effects on walking, even when wrapped around a motor nerve. Moreover, NBAT is actively driven by ultrasound application, ensuring swift and reversible pain control. This work offers a promising avenue for managing acute postoperative pain, obviating the necessity for secondary surgical removal as it naturally dissolves over time.

Materials and structure design of NBAT

Figure 1a,b depicts NBAT, which address the limitations of conventional pain control method with circular cuff electrodes. Conventional method, reliant on lengthy cuff electrodes connected to external energy sources, impedes wound healing, strains nerves and induces mechanical stress. Conversely, NBAT, powered by safe ultrasound, generates electric field parallel to nerve, effectively managing pain. Two strategies were used to improve the performance of NBAT: (i) regulating bioresorbable polymer surface morphology for smooth contact and separation and (ii) endowing a single bioresorbable polymer material with opposite triboelectric properties through surface functionalization (Fig. 1c). Vibrating via ultrasonic waves and making the electric field through contact and separation necessitate a gap between the two materials[16–18]. To achieve enough space between the two films, we formed dimple structure via solvent exchange[19] (Extended Data Fig. 1). Poly(lactic-co-glycolic acid) (PLGA) was used as the bioresorbable polymer. Scanning electron microscopy image shows well-formed dimple structures. Also, universal testing machine analysis reveals no notable deviation in mechanical properties (Supplementary Fig. 1). For the opposite triboelectric properties, functional groups were utilized; poly-L-lysine imparted tribopositive properties, while trichloro(1*H*,1*H*,2*H*,2*H*-perfluorooctyl) silane (FOTS) imparted tribonegative properties[20,21]. X-ray photoelectron spectroscopy (XPS) analysis (Fig. 1d and Supplementary Fig. 2) confirms PLGA surface treatment with functional groups[22]. Furthermore, contact angle data and Fourier transform infrared analysis corroborate processing of different functional groups (Supplementary Figs. 3 and 4). Pretreatment with a reactive ion etcher facilitated the uniform modification of functional groups, as demonstrated by contact angle measurements on surfaces treated versus untreated (Supplementary Fig. 5). This approach, conferring conflicting triboelectric properties via functional group treatment, exhibits consistent behaviour across various time-limited polymers beyond PLGA, allowing polymer selection based on target treatment duration in future applications (Extended Data Fig. 2).

To evaluate the efficacy of the structural and material design strategies, the electrical properties of NBAT were analysed. Kelvin probe force microscopy analysis revealed a notable difference in the work function values of the two polymers treated with distinct functional groups, indicating electron transfer between two films (Fig. 1e). The density functional theory (DFT) calculation results support the surface charge density difference between surface-functionalized PLGA polymers (Supplementary Figs. 6 and 7). Triboelectric properties were assessed using a pushing tester, confirming substantially enhanced voltage output with reversed functional group treatment on both sides and well-formed dimple structures on the FOTS-PLGA surface (Extended Data Fig. 3a). With these findings, surface charge was calculated by finite element method (FEM) to determine electric potential, demonstrating consistency with triboelectric output (Extended Data Fig. 3b). NBAT, whose structure enables the generation of the largest electric field, was fabricated using a thermal combination (Fig. 1f and Extended Data Fig. 4). The XPS analysis indicates maintained functional groups after heat treatment (Supplementary Fig. 8). Biodegradability of the device was assessed in in vitro and in vivo environments[23]. Single film biodegradation speeds, treated with diverse functional groups in a 37 °C phosphate-buffered saline (PBS) buffer solution, exhibited uniformity (Supplementary Figs. 9 and 10). Daily ultrasound stimulation (0.5 W cm^{-2} for 30 min) did not alter the degradation rate of NBAT in in vitro conditions, indicating that ultrasound exposure does not affect the resorption behaviour of the polymer (Supplementary Fig. 11). This observation is consistent with our previous findings that low-intensity ultrasound does not influence polymer degradation, whereas high-intensity ultrasound can accelerate degradation rates[17]. NBAT's biodegradation speed in the same environment demonstrated complete degradation within 4 weeks (Extended Data Fig. 5a). In addition, to determine the biodegradability in an in vivo environment, NBAT was implanted and wrapped around a nerve (Fig. 1g). It was confirmed that the NBAT was almost completely biodegraded after about 30 days even in an in vivo environment (Extended Data Fig. 5b).

Biocompatibility and behaviour analysis

To verify biocompatibility of each surface-functionalized PLGA layer, we compared the viability of fibroblast cells (CRL-1502) that is cultured with bare PLGA, FOTS-PLGA and poly-L-lysine PLGA through 3-{4,5-dimethylthiazol-2-thiazolyl}−2,5-diphenyl-2*H*-tetrazolium bromide (MTT) assay for 72 h (Fig. 2a). Compared with the bare PLGA group, surface-functionalized groups showed slightly higher cell viability, which indicates that the influence of surface functionalization on cell viability was negligible. The results in Fig. 2b indicate that the viability of CRL-1502 is cultured with NBAT for 72 h. As shown in Supplementary Fig. 12, immunofluorescent staining results revealed no distinguishable differences in proliferation or morphology between control and NBAT groups at both 24 h and 48 h post-implantation. Similarly, at 72 h post-implantation, there was no notable difference in cell viability observed between control and NBAT groups (Fig. 2b). A gait analysis was performed to determine whether device implantation around the nerve impacts gait of rats. The gait along straight maze was recorded (Supplementary Video 1), and its patterns were evaluated with three parameters: gait height, stride and toe-off phase (Fig. 2c–e). All parameters were derived from previous studies, including analysis related to behavioural and neurological states[24]. In Fig. 2c, NBAT-implanted rats showed normal gait in terms of gait height and stride with the control group. With regard to the toe-off phase, Fig. 2d shows the ankle angle and Fig. 2e shows the

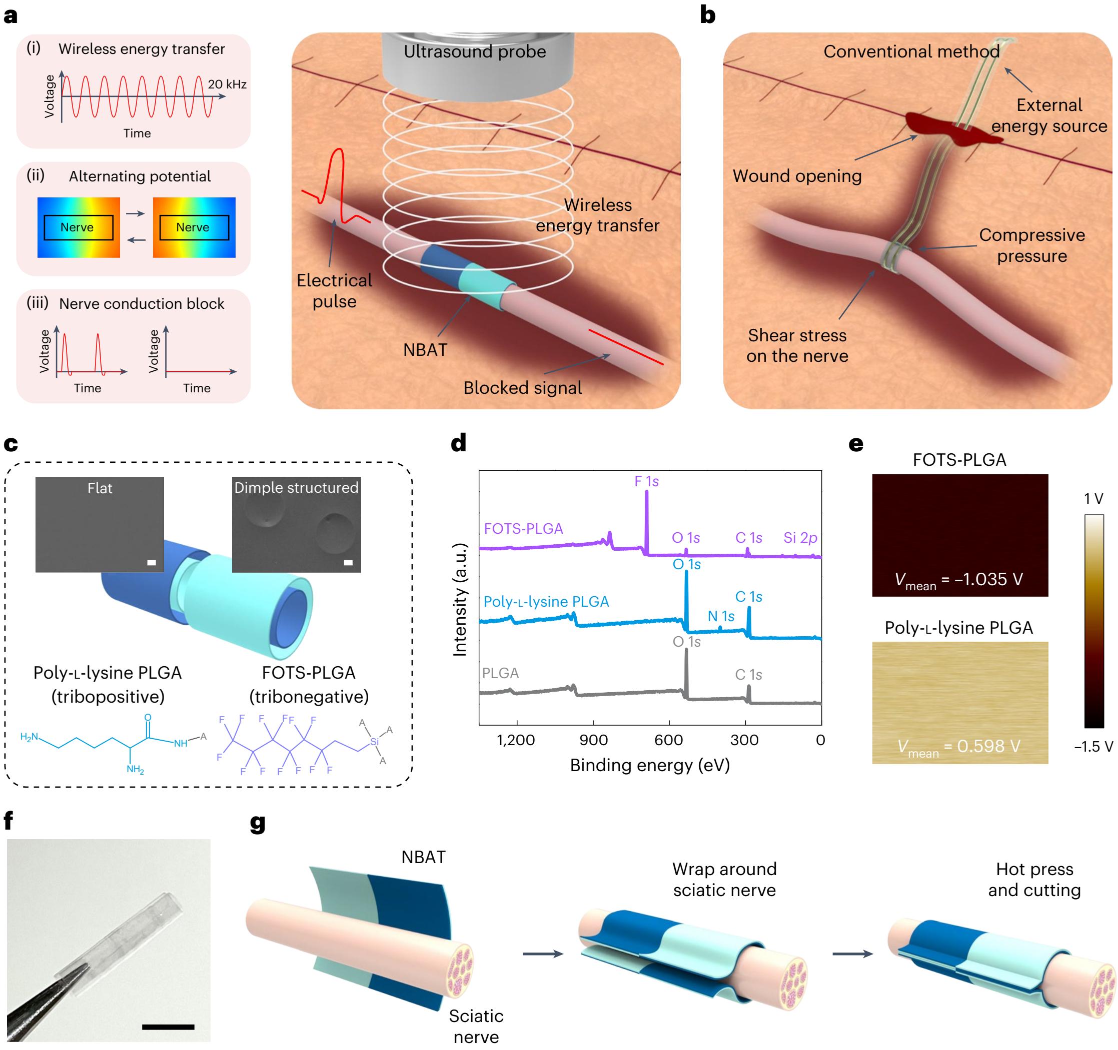

Fig. 1 | Design of a wireless, electrode-free and bioresorbable nerve block system. a, Each rectangular box is associated with the procedure of nerve block mechanism (left). Schematic of NBAT integrated with the nerve (right). **b**, Conventional nerve block system with circular cuff electrodes powered by wired external power source. **c**, Schematic and layer assembly of NBAT for generating alternating potential aligned with nerve. The notation 'A' in the chemical structure represents PLGA. The inset scanning electron microscopy images indicate surface morphology of each layer. Scale bars, 10 µm. **d**, XPS analysis of the surface-functionalized PLGAs. **e**, Surface potential characterization of the surface-functionalized PLGAs. **f**, Photograph of NBAT. Scale bar, 0.5 cm. **g**, Schematic illustrations of overall procedures of implantation of NBAT.

normalized ankle angle, demonstrating no difference between them[25] (Supplementary Fig. 13). NBAT-implanted rats showed similar results to the control group in the rotarod test and had no behavioural problems (Supplementary Fig. 14 and Supplementary Video 2). To evaluate the mechanical burden imposed on nerves by different devices, we performed FEM simulations comparing a conventional rigid cuff electrode and the soft NBAT. The commercial cuff, owing to its stiffness and tendency to retain its original shape, applied notable compressive stress to the nerve when wrapped. By contrast, NBAT, made of a flexible and compliant polymer, closely conformed to the nerve without generating noticeable stress. These results suggest that NBAT minimizes mechanical load during implantation, reducing the risk of nerve damage (Supplementary Fig. 15).

Figure 2f–j shows blood component analysis after 1-month implantation of NBAT. All five main parameters, red blood cell (RBC), white blood cell (WBC), platelet (PLT), aspartate aminotransferase (AST) and alanine aminotransferase (ALT), were within normal ranges, with negligible differences compared with the control group[26]. Other parameters were also observed to have no important differences from the control group, as illustrated in Supplementary Fig. 16. Given that key components of NBAT fully dissolve within 4 weeks, this result indicates an absence of toxic effects (Supplementary Figs. 17 and 18). For histological analysis, we carried out haematoxylin and eosin (H&E)-stained sections of implant sites, surrounding tissues and major organs (heart, spleen, lung, liver and kidney). Figure 2k and Supplementary Fig. 19 show no discernible immune reactions related to implantation (week 1) and degradation of NBAT (week 4). These cell viability, gait, blood and histology results all supported that NBAT is able to be implanted on the sciatic nerve with minimal negative influence on rats.

Electrical characterization and nerve block mechanism of NBAT

The arrangement of polymers comprising NBAT facilitates the creation of an alternating electric field oriented parallel to the nerve. Electrical analysis methods were used to comprehensively understand NBAT's mechanism in blocking nerve signals through alternating electric fields (Fig. 3). NBAT was designed by leveraging principles from the existing KHFAC method. Unlike the conventional KHFAC method, which utilizes bipolar electrodes connected externally to directly apply alternating current signals to nerves, NBAT generates

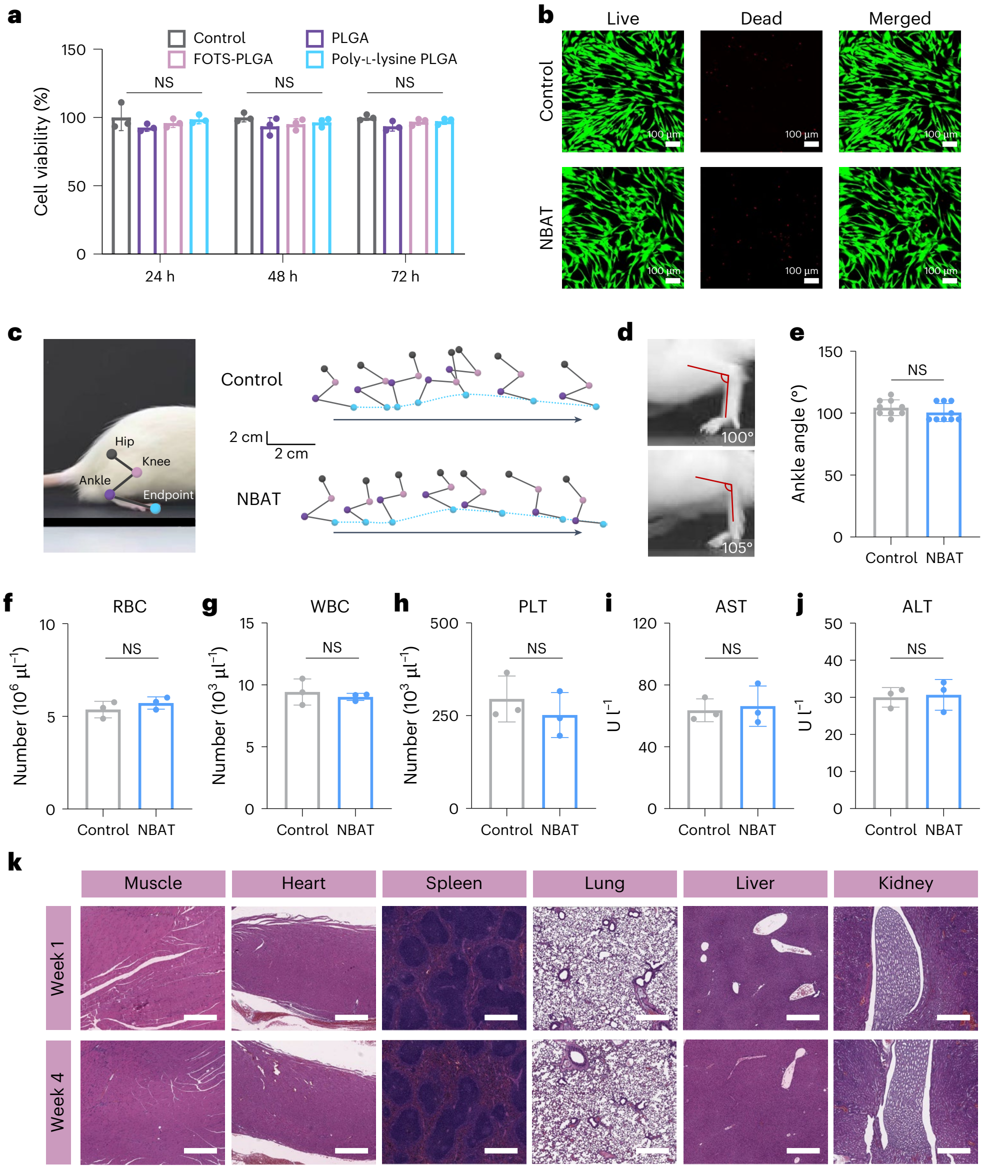

Fig. 2 | Behaviour study and biocompatibility of NBAT. a, Relative cell viability of fibroblasts (CRL-1502) on the surface-functionalized bioresorbable polymers for 24 h, 48 h and 72 h ($n = 3$ biologically independent samples; each averaged from 8 technical replicates, mean ± s.d.). For each time point, cell viability was normalized to the control group (set as 100). **b**, Representative fluorescence microscopy images of live/dead staining of CRL-1502 cells cultured on the NBAT for 72 h. Scale bars, 100 μm. **c**, Hindlimb kinetics during walking (left). Stick diagram decompositions of hindlimb movements (right). Scale bar, 2 cm. **d**,**e**, Photograph (**d**) and histogram of normalized angle (**e**) of the ankle angle toe-off phase test ($n = 3$ biologically independent samples; each subject was measured in three technical replicates, mean ± s.d. (see details in Supplementary Fig. 13)). **f**–**j**, Histogram showing CBC and serum test RBC (**f**), WBC (**g**), PLT (**h**), AST (**i**) and ALT (**j**). Control group refers to subjects without NBAT implantation ($n = 3$ biologically independent samples, mean ± s.d.). **k**, Histological images of the muscle, heart, spleen, lung, liver and kidney tissues stained with H&E of the 1-week and 4-week groups. Scale bars, 500 μm ($n = 3$ biologically independent samples, mean ± s.d. (see details in Supplementary Fig. 19)). *P* values were evaluated through a two-sided Student's *t*-test; NS, non-significant. Exact statistical values are provided in Supplementary Table 1.

an electric field by crossing the films. As ultrasound waves transmit, an electric field fluctuates at the same frequency as the ultrasound waves are generated. Changing electric field can influence the movement of ions within the nerve. To quantitatively analyse the surface charge formed by NBAT, triboelectric output was measured under 0.5 W cm^{-2} intensity of ultrasound (Supplementary Figs. 20 and 21). When the output was tested after overlapping the films in reverse, output of different phases was obtained, and this result confirmed the possibility of forming an electric field parallel to the nerve (Supplementary Fig. 22). In addition, NBAT's output showed the same output even after about a week, confirming that the effect of surface treatment lasts for a long time (Supplementary Fig. 23). Supplementary Fig. 24 is the result of measuring the output by wrapping NBAT around an electrode with a resistance similar to that of a nerve. The active area decreased, and the output also decreased, but valid output was measured. We confirmed that similar output was seen when using real nerves as electrodes. Electrodes for measurement were wrapped around both sides of the NBAT to assess the electrical energy generated as the film vibrates (Fig. 3a). Subsequently, ultrasound with an intensity of 0.5 W cm^{-2} was applied to measure the open circuit voltage at the electrode. Analysis of the electrical output of NBAT from each electrode revealed outputs with opposite phases (Fig. 3b). While the voltage measured at each electrode is approximately 2 V, the combined output with opposite phases perceived by the nerve can reach up to 4 V.

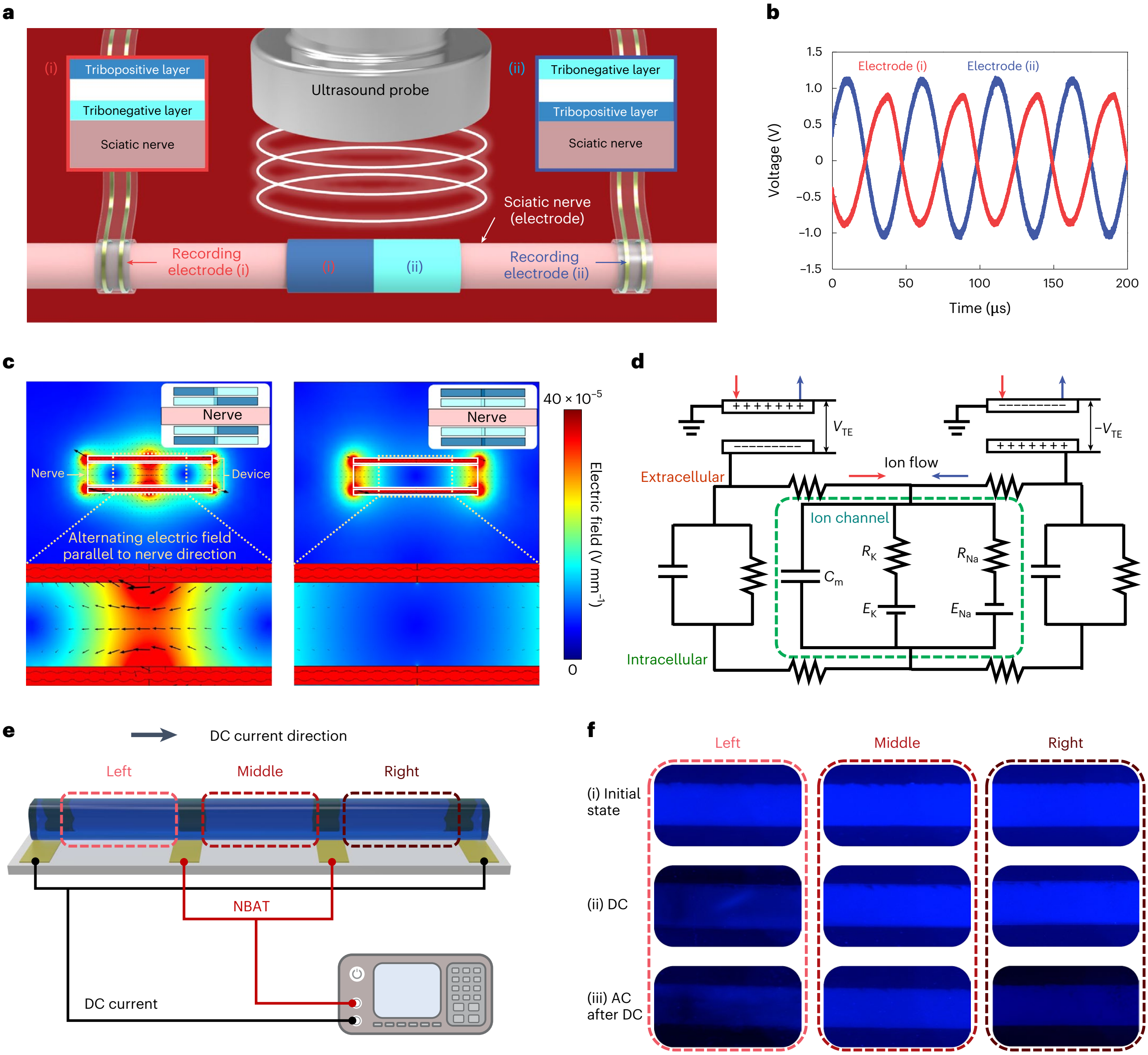

Fig. 3 | Working mechanism demonstration of NBAT. a, Schematic illustration of experimental set-up for demonstrating phase difference. **b**, Phase difference of between electrodes (i) and (ii). **c**, FEM simulations of NBAT structure (left) and non-intersecting structure (right). The inset images indicate the structure of each structure. **d**, Circuit diagram of NBAT integrated with nerve. The green box represents the ion channel of nerve. **e**, Schematic illustration of experimental set-up for ion movement by alternating electric field. **f**, Epifluorescence microscopy images of each case.

FEM simulations were conducted to evaluate the structural effect of NBAT. When opposing potentials with the same frequency as ultrasound form around the nerve, a robust electric field parallel to the nerve is established at the centre of the film (Fig. 3c, left, and Supplementary Fig. 25). However, merely overlapping films with opposite electrostatic properties results in the inability to form an electric field inside the nerve (Fig. 3c, right). On the basis of these electrical characteristics, a circuit model of NBAT was proposed. As the film forming the electrical potential vibrates under ultrasound and alters the electric field, sodium and potassium ions (Na^+ and K^+, respectively) surrounding the nerve are affected (Fig. 3d). Typically, ions, whose movement is governed solely by ion channels, are influenced by the alternating electric field. The electric field generated parallel to the nerve induces constant vibration of ions in place, hindering their movement around the ion channel (Supplementary Figs. 26 and 27). Consequently, the ions are unable to traverse the channel, impeding the transmission of electrical signals along the nerve. We performed an experiment to determine how NBAT affects the movement of ions (Fig. 3e). Initially, without any electric field, the ions were evenly distributed and showed similar brightness across all locations (Fig. 3f). However, when a DC current was applied from left to right, the ion concentration decreased on the left as the ions moved to the right, and the epifluorescence microscopy image darkened accordingly. Afterwards, when an AC electric field at the NBAT output level was applied, the ions moving to the right stopped and accumulated in the centre owing to the influence of the AC electric field, leading to decreased ion concentrations on both the right and left sides. This confirmed that the AC electric field generated by NBAT can affect the movement of ions.

Nerve blocking efficacy of NBAT

NBAT, which adopts the existing KHFAC method, possesses the same reversible ability to block nerve signals (Fig. 4). Rat and porcine models were used to verify the nerve conduction blocking efficiency of NBAT. Similar to the electrical output measurement experiment, bipolar stimulation and recording electrodes were wrapped around both sides of the NBAT, and a square wave pulse signal (1 Hz, 1.2 V, 1 ms) was delivered to the nerve through the stimulation electrode (Fig. 4a,b). As per the described mechanism, NBAT retards the movement of ions around the nerve, gradually impeding nerve signals. To quantify these effects, we used standard electrophysiological recording techniques to monitor changes in compound action potentials and validate NBAT-induced signal suppression (Supplementary Fig. 28). To ascertain changes in ion movement, alterations in action potential were examined. Before NBAT was activated by ultrasound, the electrical signal transmitted through the stimulation electrode induced an action potential in the proximal sciatic nerve, yet its magnitude gradually declined upon NBAT activation (Fig. 4c). The nerve potential measured at 1 s intervals progressively diminished as ion movement decreased (Fig. 4d). Consequently, upon NBAT activation, the threshold voltage cannot be exceeded even with electrical stimulation, hindering normal formation of the action potential owing to depolarization, thereby blocking nerve signals. We measured changes in compound muscle action potential (CMAP) and compound nerve action potential (CNAP) to determine whether the electrical signals transmitted through the nerves could be blocked by NBAT (Fig. 4e and Extended Data Figs. 6 and 7). The sciatic nerve used in the experiment is a mixed nerve containing both sensory and motor fibres, so blocking nerve signals can reduce both CMAP and CNAP. All electrophysiological signals were recorded using surface or needle electrodes connected to a standard amplifier and digitizer system, enabling real-time monitoring of amplitude and latency shifts during stimulation. By comparing the control group, the ultrasound (US) group where only ultrasound was applied, the sham group and the groups in which NBAT was activated by ultrasound, we found that CMAP and CNAP values decreased only when ultrasound was applied to NBAT (Fig. 4f,g). The reversibility of nerves whose signals were blocked via NBAT was validated through changes in cross-sectional images measured using a transmission electron microscope (TEM) (Fig. 4h). These images depict no nerve damage even after an hour of signal blockage via NBAT. To further assess the temporal resolution of the electrophysiological response, we conducted high-frequency sampling of CNAPs at 3 s intervals following ultrasound activation. Following ultrasound activation, CNAP amplitude rapidly diminished, reaching a minimum within 6 s. Upon cessation of ultrasound, the signal recovered to baseline within another 6 s, confirming the reversible and rapid blocking behaviour of NBAT (Fig. 4i). Subsequently, we verified whether nerve signals were electrically blocked through repeated experiments under the same conditions. Upon applying ultrasound to the NBAT, the voltage of the nerve, initially measured at an average of 0.35 V, decreased by more than 85% (Supplementary Fig. 29). Also, this blocking effect was demonstrated in the porcine model (Fig. 4k). The stimulation pulse signal was completely blocked from approximately 0.08 V to 0 V (Fig. 4l,m). More complete nerve conduction blocking was observed in the porcine model compared with the rat model. While thicker nerves generally lead to reduced current density in conventional current-driven systems owing to increased cross-sectional area, NBAT operates via a triboelectric field-based mechanism rather than direct current injection. In this system, the generated electric potential increases proportionally with the surface area of the nerve, and the electric field across the nerve scales approximately with the radius. As a result, larger nerves provide greater active area for surface charge generation and yield stronger local electric fields. This geometry-dependent enhancement is consistent with the working principles of triboelectric nanogenerators and explains the improved blocking efficiency observed in the porcine model. Collectively, these electrophysiological measurements confirm that NBAT is capable of robust, reversible and temporally controlled modulation of peripheral nerve activity across species.

Histological validation of long-term safety and behavioural evidence of acute pain relief with NBAT

To address the critical need for translational evidence in non-pharmacological neuromodulation, we assessed long-term safety and acute pain-relieving efficacy of NBAT in vivo using histological, behavioural and tracking-based evaluations (Fig. 5). Histological analysis was performed to evaluate chronic immune response and fibrosis following NBAT implantation. Sciatic nerves were collected at 2 and 4 weeks post-implantation and stained using Masson's trichrome (for collagen deposition), CD45 (a pan-leukocyte marker for inflammation) and α-smooth muscle actin (α-SMA; for fibrotic transition). As shown in Fig. 5a, CD45-positive immune cell infiltration remained negligible at both time points, indicating minimal inflammatory response from foreign body reaction. α-SMA-positive myofibroblasts were sparsely observed around the nerve boundary, but not within the nerve parenchyma, and did not increase over time, suggesting the absence of progressive fibrotic encapsulation. Notably, Masson's trichrome staining revealed no internal collagen accumulation or epineurial thickening within the nerve, confirming that NBAT implantation did not cause chronic scarring or tissue remodelling, even after prolonged in vivo degradation. These results support the high biocompatibility and mechanical compliance of NBAT with peripheral nerves, overcoming concerns raised by conventional cuff systems that induce compression-related neuropathy. To further examine potential off-target tissue responses, we conducted histological evaluations on muscle tissues surrounding the sciatic nerve following NBAT implantation and ultrasound stimulation. At both 2 and 4 weeks post-implantation, Masson's trichrome, CD45 and α-SMA staining of perineural muscle sections revealed no abnormal collagen deposition, immune cell infiltration or fibrotic remodelling, respectively. These findings are consistent with nerve histology and confirm that NBAT does not induce adverse inflammatory or fibrotic responses in adjacent muscular tissues over time (Supplementary Fig. 30).

To validate pain modulation by NBAT, we used a sciatic nerve crush injury model—an established acute pain model characterized by heightened sensitivity and movement suppression owing to sensory fibre disruption (Fig. 5b, left). After injury, rats were placed in a 40 cm × 40 cm open-field arena and tracked for 30 min using video analysis (Fig. 5b, right). Behavioural activity was quantified in terms of average movement velocity and total travel distance (Fig. 5c,d). The control, ultrasound-only (US) and sham (NBAT without ultrasound) groups all showed reduced locomotion, consistent with acute nociceptive behaviour. By contrast, the NBAT group—which received ultrasound activation 2 days post-injury—exhibited a significant increase in both average velocity and travel distance, indicating effective suppression of pain-related movement inhibition. Importantly, the NBAT group restored exploratory behaviour comparable to uninjured animals, which is strongly suggestive of nociceptive signal blockade from unmyelinated C-fibres, even though their electrical signals cannot be directly measured using CMAP or CNAP. While CMAP suppression demonstrates motor pathway involvement (Fig. 4), this behavioural improvement offers indirect yet functional evidence of NBAT-mediated sensory pain relief. Trajectory analysis of the open-field behaviour further reinforces this finding. As shown in Fig. 5e and Extended Data Fig. 8, rats in the control, US and sham groups exhibited restricted movement, primarily confined to corners—a known indicator of pain-induced anxiety and limited mobility. By contrast, the NBAT group showed widespread locomotion across the chamber, reflecting normalized behaviour and alleviated discomfort. These behavioural data satisfy the requirement of using a validated pain model, confirm sensory pathway

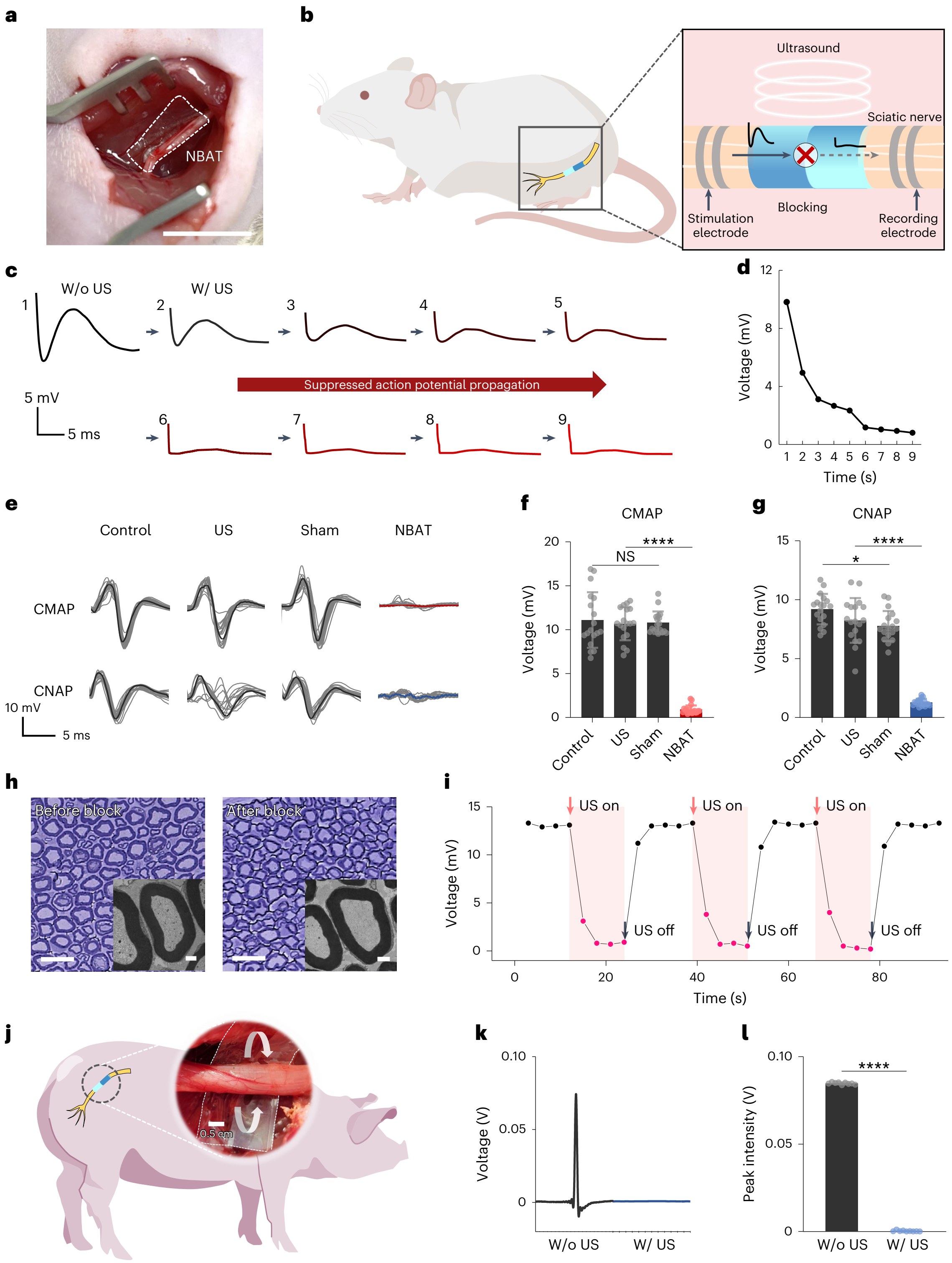

Fig. 4 | In vivo tests for nerve conduction block with NBAT. a, Photograph of NBAT integrated with the sciatic nerve of rat. Scale bar, 1 cm. **b**, Schematic illustration of experimental set-up. **c**, Suppression of compound action potential propagation with US activation (intensity 0.5 W cm^{-2}, frequency 20 kHz). **d**, Line graphs of action potential amplitude change over US activation time. **e**, Line graphs of CMAP and CNAP measurement ($n = 18$ for each group). **f**,**g**, Peak intensity analysis of CMAP (**f**) and CNAP (**g**) ($n = 18$ biologically independent samples; each subject was measured once, mean ± s.d.). **h**, Cross-sectional semi-thin images of the sciatic nerve of rat before (left) and after (right) electrical nerve block. Scale bars, 20 µm. Each inset image indicates the TEM image of the sciatic nerve of rat. Scale bars, 2 µm. **i**, Time-resolved CNAP amplitude changes upon ultrasound activation. CNAP peak amplitude was recorded every 3 s before, during and after ultrasound stimulation. **j**, Schematic and photograph of NBAT integrated with the sciatic nerve of pig. **k**, Peak analysis before and after US activation in a porcine model. **l**, Peak intensity analysis before and after US activation in a porcine model ($n = 3$ biologically independent samples; the subject was measured three times, mean ± s.d.). *P* values were evaluated through a two-sided Student's *t*-test; $^{*}P < 0.05$; $^{****}P < 0.0001$. Exact statistical values are provided in Supplementary Table 1.

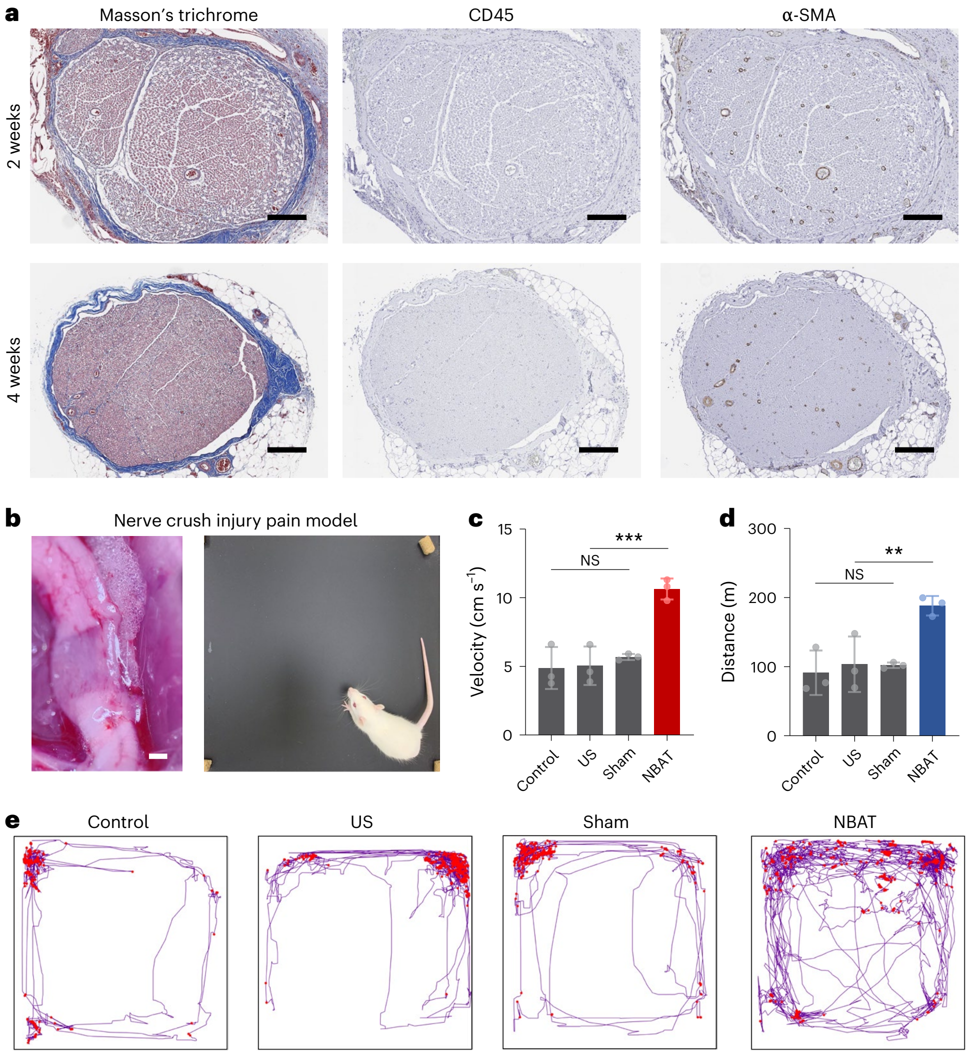

Fig. 5 | Histological and behavioural evidence for pain modulation via NBAT. a, Histological section of sciatic nerves collected at 2 and 4 weeks post-implantation, stained with Masson's trichrome (collagen in blue), CD45 (inflammatory cells) and α-SMA (fibrosis marker). NBAT did not induce inflammatory infiltration or fibrotic encapsulation. Scale bars, 200 µm. **b**, Left: photograph of the sciatic nerve crush injury model used to induce acute pain. Scale bar, 1 mm. Right: open-field behavioural testing set-up (40 cm × 40 cm chamber) used to evaluate locomotor behaviour. **c**, Average movement velocity in different groups: control, ultrasound-only (US), sham (NBAT without ultrasound) and NBAT (ultrasound-activated) ($n = 3$ biologically independent samples; each subject was measured once, mean ± s.d.). **d**, Total movement distance during a 5 min session. NBAT group showed significantly enhanced locomotion ($n = 3$; each subject was measured once, mean ± s.d.). **e**, Representative movement trajectories of rats in each group during open-field testing. NBAT-treated animals demonstrated considerably greater exploratory behaviour. *P* values were evaluated through a two-sided Student's *t*-test; $^{**}P < 0.01$; $^{***}P < 0.001$. Exact statistical values are provided in Supplementary Table 1.

engagement and provide functional proof of concept for acute pain control via NBAT. Together, these results establish that NBAT enables safe, reversible and effective suppression of pain-associated behaviour in an acute injury model. Importantly, this is achieved without inducing chronic inflammation or fibrosis, thereby demonstrating the translational potential of this fully bioresorbable neuromodulation system for temporary postoperative pain relief.

Conclusion

We presented a wireless, electrodeless and bioresorbable nerve block system based on alternating triboelectric potential (NBAT) capable of immediate and reversible pain control. The system is non-invasively activated by ultrasound, enabling spatiotemporally controlled neuromodulation without the need for external electrodes or wires. By utilizing a triboelectric design, NBAT generates opposing surface potentials across a single polymer film, forming an alternating electric field aligned with the nerve direction. Compared with conventional systems, NBAT offers several critical advantages: (1) minimal mechanical burden on the nerve without shear or compressive stress, (2) complete closure of the skin incision without external wiring and (3) full biodegradability of the monomaterial structure. This design simplifies the implantation procedure and eliminates the need for device retrieval surgery. In vitro and in vivo assessments confirmed the biocompatibility and biodegradation profile of the system. Notably, long-term histological analysis using Masson's trichrome, CD45 and α-SMA staining revealed no considerable immune cell infiltration, fibrosis or collagen accumulation in the nerve or surrounding muscle after 2 and 4 weeks of implantation. These findings validate the chronic biocompatibility of NBAT. In addition, behavioural evaluation in a rat sciatic nerve crush injury model confirmed functional recovery and pain alleviation. NBAT-treated animals exhibited significantly increased locomotion and velocity in open-field tests, compared with control, ultrasound-only and sham groups. These behavioural outcomes suggest effective suppression of pain-related responses likely mediated by NBAT-induced blockade of sensory fibres, particularly small unmyelinated C-fibres not measurable by motor-dominant electrophysiology alone. Together, these results demonstrate that NBAT is a safe, soft and fully bioresorbable neuromodulation system suitable for temporary implantation in postoperative pain management. Its ability to deliver reversible analgesia without drugs or rigid electronics represents a promising strategy for preventing opioid overuse and accelerating recovery. The use of bioresorbable polymers with tunable degradation timelines, combined with the endogenous conductivity of nerves, suggests that NBAT can be readily adapted for broader clinical applications in acute or subacute pain therapy.

Methods

Materials synthesis and surface functionalization

PLGA (lactide/glycolide 65:35; M_w 40,000–75,000, weight-average molecular weight) was obtained from Sigma-Aldrich. PLGA film preparation began with dissolving 0.1 g PLGA in 2 ml chloroform. The solution was stirred at room temperature for 30 min to make a fully dissolved solution. The solution was drop-cast on the substrate and first dried at 50 °C for 5 min and then in ambient conditions. In the case of dimple-structured PLGA, the solution was drop-cast on the substrate and dried at 50 °C for 5 min and then in humid conditions. For the surface-functionalized film, the dried film was peeled off and cleaned with deionized water gently, followed by treatment in oxygen plasma (O_2, radio frequency power, 8 sccm, 80 W, 300 s). In the case of FOTS (97%, Sigma-Aldrich)-PLGA, the film was put in a container by dropping a few FOTS drops and was placed in the oven at 40 °C for 3 h. For the poly-L-lysine PLGA, the oxygen plasma-treated film was soaked in a poly-L-lysine solution (0.1% in H_2O, Sigma-Aldrich) for 24 h. Subsequently, the poly-L-lysine PLGA was washed with deionized water and dried.

Materials analysis

XPS (UVP, NEXSA G2), Fourier transform infrared (Bruker, VERTEX 70) analysis and contact angle analysis were performed to analyse chemical structures of PLGA, FOTS-PLGA and poly-L-lysine PLGA. The surface morphology of flat PLGA and dimple-structured PLGA was observed by field-emission scanning electron microscopy (FE-SEM, Jeol, JSM-7610F-Plus). The mechanical property of dimple-structured PLGA was analysed using a universal testing machine (INSTRON, 5844). The surface potential was investigated through a Kelvin probe force microscopy (Park Systems, XE-100) system with a Pt/Cr-coated silicon tip and lock-in amplifier (Stanford Research, SR830).

Device fabrication

Extended Data Fig. 4 provides a schematic of a device fabrication process. NBAT is composed of FOTS-PLGA with dimple structure as a tribonegative layer and poly-L-lysine PLGA as a tribopositive layer. Each layer (thickness of 20 µm) was cut into the desired shape and polytetrafluoroethylene layer to be put in the middle was also cut into the desired shape. Two kinds of PLGA layer overlap a certain area (splice) and the splice area was integrated using heat. Then the two integrated films were subsequently integrated with overlapped edge.

MTT assay

The MTT assay was performed using human fibroblast cells (ATCC, CRL-1502) with experimental films sized 3 × 3 mm placed in a 96-well plate. Each well was inoculated with 10,000 cells suspended in 100 µl of culture medium and subjected to incubation periods of 24 h, 48 h and 72 h. After incubation, the medium was replaced with 50 µl of serum-free medium and 50 µl of MTT reagent (5 mg ml^{-1}, Abcam, ab146345), and incubation continued for 2 h at 37 °C. Following this, the mixture was discarded, wells were washed with diluted PBS, and 150 µl of dimethyl sulfoxide (Sigma-Aldrich, D8418) was added to each well for 15 min to solubilize the formazan. Finally, 100 µl from each well was transferred to a new 96-well plate for absorbance measurement at 570 nm to assess cell viability.

Live/dead assay

Live/dead assays were conducted utilizing the LIVE/DEAD Cell Imaging kit (Invitrogen, R37601), adhering strictly to the guidelines provided in the operational manual. Cells were treated with an equal volume of 2× working solution and incubated for 20 min at room temperature. Fluorescence microscopy images were captured using 20× objectives on a Zeiss LSM 700 or 780 confocal microscope.

H&E staining

The tissues were fixed using 4% formaldehyde for 24 h at a temperature of 4 °C. Following fixation, the tissues were washed in PBS at room temperature. After washing, the tissues were dehydrated in ethanol, cleared in xylene and embedded in paraffin wax. Serial sections of 5 µm thickness were cut from the embedded tissues and applied to microscope slides for staining purposes. Thin sections were stained with H&E to assess tissue damage and inflammation.

CBC test

Complete blood count (CBC) analysis is conducted by collecting whole blood samples into tubes containing ethylenediaminetetraacetic acid, an anticoagulant that preserves the blood's integrity. These samples are then analysed using an automated haematology analyser (ProCyte DX haematology analyser; IDEXX Laboratories). This analysis accurately measures various blood parameters, including red and white blood cells, platelets, haemoglobin and haematocrit, offering a comprehensive overview of the subjects' haematological health.

Serum chemistry analysis

Serum chemistry analyses were conducted using the Fuji DRI-Chem NX500i system (FUJIFILM). Serum samples, obtained by centrifuging whole blood at 1,500 × *g* for 10 min, were analysed to evaluate various biochemical parameters.

Behaviour analysis: ankle angle toe-off phase, rotarod

To evaluate NBAT implantation effect on gait of rats, ankle angle at toe-off phase and rotarod test were performed at postoperative 7 days using straight maze. In brief, three rats were placed in walking track (length, 1 m; width, 20 cm; height, 20 cm). During walking, a video was acquired with a digital camera at a distance of 1 m and calibrated to prevent optical distortion. Lines of leg and foot segments were identified and the ankle angle at the toe-off phase was measured at the moment of maximal plantar flexion of ankle joint and expressed in degrees. During the adaptation phase, the animals were subjected to training sessions 3 times per day at a speed of 10 rpm for 3 consecutive days. Their ability to stay on the rotarod (LE8205, Panlab) was measured by noting the time until they fell at a set speed of 20 rpm, with this process repeated 3 times during a period of 3 min. The rotarod assessment was carried out thrice for every animal, and the mean of these three values was computed to determine the outcome.

Ion movement test using fluorescent staining

To demonstrate restricted ion movement under AC electric field, cellulose paper soaked in a 1 M NaCl (Sigma-Aldrich, S9625) solution was used. Selective staining Na^+ ions was conducted using sodium-binding benzofuran isophthalate (SBFI) (ThermoFisher, S1262). After dipping the cellulose paper, which was exposed to NaCl solution, in SBFI working solution for 5 min, it was gently washed with deionized water. The movement of stained Na^+ ions can be observed using light with 380 nm wavelength. DC current was applied to both ends of the stained cellulose paper, while an AC electric field at the same level as NBAT was applied to the centre to control the movement of Na^+

ions. DC power supply (UNI-T, UTP1306S) and waveform generator (Tektronix, AFG1062) were utilized to exert DC current and AC electric field, respectively.

Semi-thin and TEM

Sciatic nerves collected from rats were first fixed in a solution of 2% paraformaldehyde and 2.5% glutaraldehyde in 0.1 M phosphate buffer, and then washed in the same buffer. For light microscopy, sections were stained with toluidine blue, while for electron microscopy, sections were enhanced with uranyl acetate and lead citrate. The specimens were also treated with 1% osmium tetroxide, dehydrated in ethanol, transitioned through propylene oxide and embedded in epoxy resin for both types of microscopy. Pathological evaluation was conducted on semi-thin sections for light microscopy and ultra-thin sections for electron microscopy, using specific staining and a TEM (HT7700, Hitachi) operating at 100 kV.

Experimental subjects

Animal experiments were performed using healthy adult Sprague-Dawley rats (8–9 weeks, female, 250–320 g) and pigs (*Sus scrofa domesticus*; Landrace × Yorkshire × Duroc, LYD) (10 weeks old, male, 30 ± 2 kg) were obtained from XPbio (Korea). A rat-based study was reviewed and approved by the Institutional Animal Care and Use Committee (IACUC) of Samsung Medical Center (20240109001). Subsequently, a large animal study using pig was reviewed and approved by the IACUC of BIOSTEP (23-KE-0493). All procedures were performed following guidelines established by the National Institutes of Health. At the end of experiments, rats were euthanized using CO_2 gas.

Electrophysiology test (rat and pig)—nerve conduction block

Before the nerve conduction block study, surgical procedure was followed. All procedures were conducted under anaesthesia initially induced with isoflurane 5% and O_2 0.3–0.5 l min^{-1} for 3 min, and then maintained with 2–2.5% isoflurane. The block stimuli were provided by NBAT, producing electric field with a 20 kHz sinusoidal waveform, parallel to the nerve under a 0.5 W cm^{-2} ultrasound (Mirae, MV100) intensity. Stimulation electrode was placed to the left of NBAT. The stimuli were provided by a waveform generator (Tektronix, AFG1062) generating 1.2 V, 1 Hz, square-wave pulses. Recording electrode was placed to the right of NBAT. Finally, the recorded stimuli were observed using an oscilloscope (Tektronix, DPO3052) and a probe (Tektronix, P5100A) with a 40 megohm input impedance.

For action potential, the stimuli were provided by a Nicolet VikingQuest device (Natus Medical), producing single square-wave pulses of 0.1 ms duration. The generated stimulation pulses and the CNAP signal were amplified and recorded. By using the NBAT to block nerve conduction, we observed the absence or presence of action potentials in response to the stimulus pulses.

In vitro/in vivo transient process

To assess the in vitro transient process, each component of NBAT and NBAT itself was immersed in diluted PBS solution (Biowest, pH 7.4) at 37 °C. The mass of each material and device was measured using an electronic scale (RADWAG, AS 220.R2 Plus) every week. The photograph of the device was taken to demonstrate the in vitro transient processes over time. Then, to confirm biodegradation characteristics of NBAT in an in vivo environment, the NBAT was implanted on the sciatic nerve of rats. The photograph of NBAT was also taken to demonstrate in vivo degradation properties every 10 days.

Electrical characterization

To demonstrate triboelectric characterization of surface-functionalized and dimple-structured PLGA, triboelectric nanogenerators and ultrasound-mediated triboelectric nanogenerators (US-TENG) with active area 1 cm × 1 cm were fabricated. The electrical generation properties of triboelectric nanogenerators were evaluated under 2 Hz, 3 kgf, using a pushing tester (Z-Tech, ZPS-100). The electrical generation properties of US-TENG were measured under a 0.5 W cm^{-2} ultrasound (Mirae, MV100) intensity. To demonstrate nerve conductivity in our NBAT, US-TENG using nerve as an electrode was fabricated and its output was evaluated under a 0.5 W cm^{-2} ultrasound intensity.

CMAP tests

Muscle action potentials were measured using a Nicolet VikingQuest device (Natus Medical), which provided single square-wave pulses with a duration of 0.1 ms. For the evaluation of CMAP, stimulation cathodes were located at two points: the sciatic notch and a site 12 mm distally along the peripheral nerve from this notch. The recording electrodes were affixed to the gastrocnemius muscle belly, while a ground electrode was placed at the base of the tail. The generated stimulation pulses and the CMAP signal were amplified and recorded. By using the NBAT to block nerve conduction, we observed the absence or presence of action potentials in response to the stimulus pulses.

CNAP tests

Nerve action potentials were measured using a Nicolet VikingQuest device (Natus Medical), which provided single square-wave pulses with a duration of 0.1 ms. For the evaluation of CNAP, stimulation cathodes were located at the proximal site in the sciatic nerve and recording electrodes were located at the distal part in the sciatic nerve, while a ground electrode was placed at the base of the tail. The generated stimulation pulses and the CNAP signal were amplified and recorded. By using the NBAT to block nerve conduction, we observed the absence or presence of action potentials in response to the stimulus pulses.

DFT calculation

Using the CASTEP module (implemented in Materials Studio), we investigated tribonegative behaviour of FOTS-PLGA and tribopositive behaviour of poly-L-lysine PLGA. Optimizing chemical structure was carried out using the BFGS algorithm with the Perdew, Burke and Ernzerhof exchange–correlation functional under the generalized gradient approximation. The force for convergence acting on the atoms during the structure optimization was maintained at <0.03 eV Å^{-1}. We used on-the-fly generation ultrasoft pseudopotential to describe the electron–ion interaction. To integrate a *k*-space in the Brillouin zone, Monkhorst–Pack special *k*-points were used. The electronic structure of each material was analysed using a plane-wave basis with cut-off energies of 600 eV.

Histological evaluation of inflammation and fibrosis

At 2 and 4 weeks after implantation, sciatic nerves were collected for histological analysis. Samples were fixed, paraffin-embedded and stained using Masson's trichrome to evaluate collagen deposition, CD45 immunostaining for immune cell infiltration and α-SMA immunostaining to detect fibrotic transition. These three stains provided complementary insight into tissue responses to NBAT over time. All images were captured using an optical microscope and assessed by a blinded investigator. Quantitative scoring confirmed minimal chronic inflammation or fibrotic encapsulation, supporting the biocompatibility of NBAT.

Pain model: rat sciatic nerve crush injury

To validate the analgesic efficacy of NBAT in a clinically relevant setting, a rat model of peripheral nerve injury was established using a controlled sciatic nerve crush. Adult Sprague-Dawley rats (8–10 weeks old) were anaesthetized with 2–5% isoflurane (induction) and maintained under 2% isoflurane (maintenance) during surgery. After shaving and sterilizing the left lateral thigh with povidone-iodine, a small skin incision was made at the mid-thigh level. The sciatic nerve was exposed via blunt dissection between the biceps femoris and gluteus muscles.

Nerve injury was induced by compressing the exposed sciatic nerve for 5 s using a HALSEY needle holder (smooth jaws, 12.5 cm total length) at the second stage of the holder driver. After implantation of NBAT (or application of the corresponding treatment in control groups), the incision was closed with muscle and skin sutures, and animals were allowed to recover for 2 days before behavioural testing.

Behavioural analysis

To assess pain-related behavioural changes, open-field locomotion analysis was performed 3 days after nerve injury. Each rat was placed individually in a 40 cm × 40 cm square arena for 30 min. Videos of animal movement were recorded from above using a GoPro Hero 12 camera. The recorded footage was processed using custom MATLAB scripts to extract trajectory data, from which locomotor parameters, including average velocity (cm s^{-1}) and total distance travelled (m), were quantified. Reductions in movement were interpreted as a behavioural correlate of pain or functional impairment, while restored movement indicated analgesic efficacy. Experimental groups included control (injury only), US (ultrasound stimulation only), sham (NBAT without ultrasound) and NBAT (NBAT with ultrasound).

Statistical analysis

Animals were randomly assigned to treatment groups, and data collection and analysis were performed in a blinded manner. No data were excluded. Results are presented as mean ± s.d., as appropriate. Statistical analyses were performed using GraphPad Prism 9 (GraphPad Software). Statistical significance was defined as $P < 0.05$. Comparisons between two groups were performed using a two-sided Student's *t*-test, and comparisons among three or more groups were performed using one-way analysis of variance followed by Tukey's honestly significant difference post hoc test.

Reproducibility

To confirm reproducibility, LIVE/DEAD assay, H&E staining, semi-thin, Masson's trichrome, CD45 and α-SMA analyses were independently repeated three times, all yielding comparable results. Transient performance of NBAT in rat was also independently repeated three times.

Reporting summary

Further information on research design is available in the Nature Portfolio Reporting Summary linked to this article.

Data availability

The data that support the findings of this study are available within the paper and its Supplementary Information. Other relevant data are available from the corresponding authors on reasonable request. Source data are provided with this paper.

References

1. Grosser, T., Woolf, C. J. & FitzGerald, G. A. Time for nonaddictive relief of pain. *Science* **355**, 1026–1027 (2017).
2. Roldan, L. M. et al. Measurement of block thresholds in kiloHertz frequency alternating current peripheral nerve block. *J. Neurosci. Methods* **315**, 48–54 (2019).
3. Lee, G. et al. A bioresorbable peripheral nerve stimulator for electronic pain block. *Sci. Adv.* **8**, eabp9169 (2022).
4. Reeder, J. T. et al. Soft, bioresorbable coolers for reversible conduction block of peripheral nerves. *Science* **377**, 109–115 (2022).
5. Kilgore, K. L. & Bhadra, N. Reversible nerve conduction block using kilohertz frequency alternating current. *Neuromodulation* **17**, 242–255 (2014).
6. Colucci, V., Strichartz, G., Jolesz, F., Vykhodtseva, N. & Hynynen, K. Focused ultrasound effects on nerve action potential in vitro. *Ultrasound Med. Biol.* **35**, 1737–1747 (2009).
7. Lee, Y.-F., Lin, C.-C., Cheng, J.-S. & Chen, G.-S. Nerve conduction block in diabetic rats using high-intensity focused ultrasound for analgesic applications. *Br. J. Anaesth.* **114**, 840–846 (2015).
8. Rwei, A. Y. et al. Ultrasound-triggered local anaesthesia. *Nat. Biomed. Eng.* **1**, 644–653 (2017).
9. Iyer, S. M. et al. Virally mediated optogenetic excitation and inhibition of pain in freely moving nontransgenic mice. *Nat. Biotechnol.* **32**, 274–278 (2014).
10. Adrianet, R. H. et al. Reviews of physiology, biochemistry and pharmacology. *Springer* **95**, 1–109 (1983).
11. Vance, C. G., Dailey, D. L., Rakel, B. A. & Sluka, K. A. Using TENS for pain control: the state of the evidence. *Pain Manag.* **4**, 197–209 (2014).
12. Sluka, K. A. & Walsh, D. Transcutaneous electrical nerve stimulation: basic science mechanisms and clinical effectiveness. *J. Pain* **4**, 109–121 (2003).
13. Ghoname, E. A. et al. Percutaneous electrical nerve stimulation: an alternative to TENS in the management of sciatica. *Pain* **83**, 193–199 (1999).
14. Bhadra, N., Vrabec, T. L., Bhadra, N. & Kilgore, K. L. Reversible conduction block in peripheral nerve using electrical waveforms. *Bioelectron. Med.* **1**, 39–54 (2018).
15. Eggers, T. et al. Combining direct current and kilohertz frequency alternating current to mitigate onset activity during electrical nerve block. *J. Neural Eng.* **18**, 046010 (2021).
16. Hinchet, R. et al. Transcutaneous ultrasound energy harvesting using capacitive triboelectric technology. *Science* **365**, 491–494 (2019).
17. Lee, D.-M. et al. Ultrasound-mediated triboelectric nanogenerator for powering on-demand transient electronics. *Sci. Adv.* **8**, eabl8423 (2022).
18. Kim, Y.-J. et al. High-performing and capacitive-matched triboelectric implants driven by ultrasound. *Adv. Mater.* **36**, 2307194 (2024).
19. Park, J. et al. Frequency-selective acoustic and haptic smart skin for dual-mode dynamic/static human-machine interface. *Sci. Adv.* **8**, eabj9220 (2022).
20. Shin, S.-H. et al. Formation of triboelectric series via atomic-level surface functionalization for triboelectric energy harvesting. *ACS Nano* **11**, 6131–6138 (2017).
21. Shin, S.-H. et al. Triboelectric charging sequence induced by surface functionalization as a method to fabricate high performance triboelectric generators. *ACS Nano* **9**, 4621–4627 (2015).
22. Zheng, Y. et al. Environmentally stable and stretchable polymer electronics enabled by surface-tethered nanostructured molecular-level protection. *Nat. Nanotechnol.* **18**, 1175–1184 (2023).
23. Zhang, Y. et al. Advances in bioresorbable materials and electronics. *Chem. Rev.* **123**, 11722–11773 (2023).
24. Liu, Y. et al. Morphing electronics enable neuromodulation in growing tissue. *Nat. Biotechnol.* **38**, 1031–1036 (2020).
25. Shin, Y. H. et al. Effect of glutaraldehyde-crosslinked cartilage acellular matrix film on anti-adhesion and nerve regeneration in a rat sciatic nerve injury model. *J. Tissue Eng. Regen. Med.* **15**, 1023–1036 (2021).
26. Delwatta, S. L. et al. Reference values for selected hematological, biochemical and physiological parameters of Sprague-Dawley rats at the Animal House, Faculty of Medicine, University of Colombo, Sri Lanka. *Anim. Models Exp. Med.* **1**, 250–254 (2018).

Acknowledgements

S.-W.K. acknowledges support from the Basic Science Research Program (RS-2022-NR070716 and RS-2020-NR049541) through the National Research Foundation of Korea (NRF) funded by the Korean government (MSIT). B.-O.C. acknowledges support from the Korean Health Technology R&D Project, Ministry of Health and Welfare (HR22C1363 and HX23C1756).

Author contributions

Y.-J.K. and S.-H.K. conceived this work. Y.-J.K., S.-H.K., B.-J.P., J.J., Y.C. and J-H.H. performed the experiments. Y.-J.K., S.-H.K., B.-J.P., J.J., D.K., Y.C., J-H.H., H.-J.Y., K.H.L., B.-O.C. and S.-W.K. participated in the interpretation of experimental findings. D.K. carried out the DFT simulations. B.-O.C. and S.-W.K. raised funding. K.H.L., B.-O.C. and S.-W.K. supervised the research. Y.-J.K., S.-H.K., B.-J.P. and S.-W.K. wrote the paper.

Competing interests

Y.-J.K., S.-H.K., B.-J.P. and S.-W.K. are inventors on the patent applications (KR/10-0102511 and US/17/888,872). The other authors declare no competing interests.

Additional information

Extended data is available for this paper at https://doi.org/10.1038/s41551-025-01579-2.

Supplementary information The online version contains supplementary material available at https://doi.org/10.1038/s41551-025-01579-2.

Correspondence and requests for materials should be addressed to Kyu Hyoung Lee, Byung-Ok Choi or Sang-Woo Kim.

Peer review information *Nature Biomedical Engineering* thanks Damiano G. Barone, Jianguo Cheng and Gerald Loeb for their contribution to the peer review of this work. Peer reviewer reports are available.

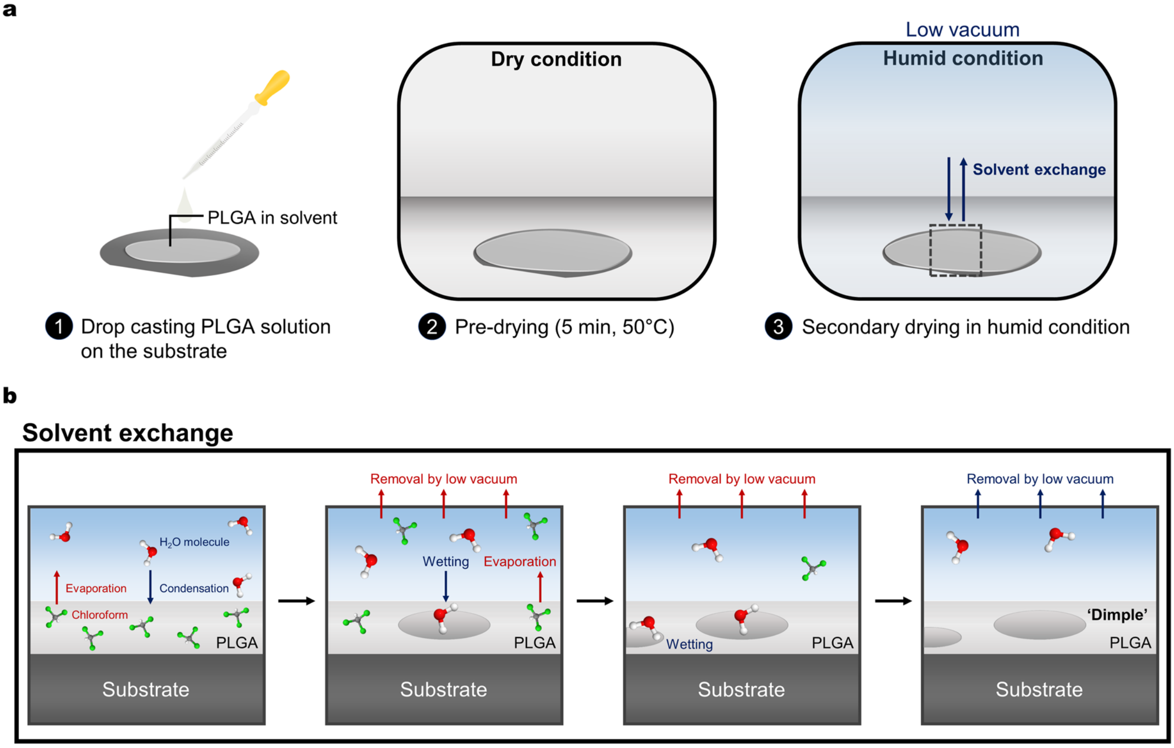

Extended Data Fig. 1 | Schematic illustrations describing solvent exchange process for dimple-structured PLGA. a Fabrication procedure of dimple-structured PLGA. **b** The principle of forming dimple-structure through solvent exchange.

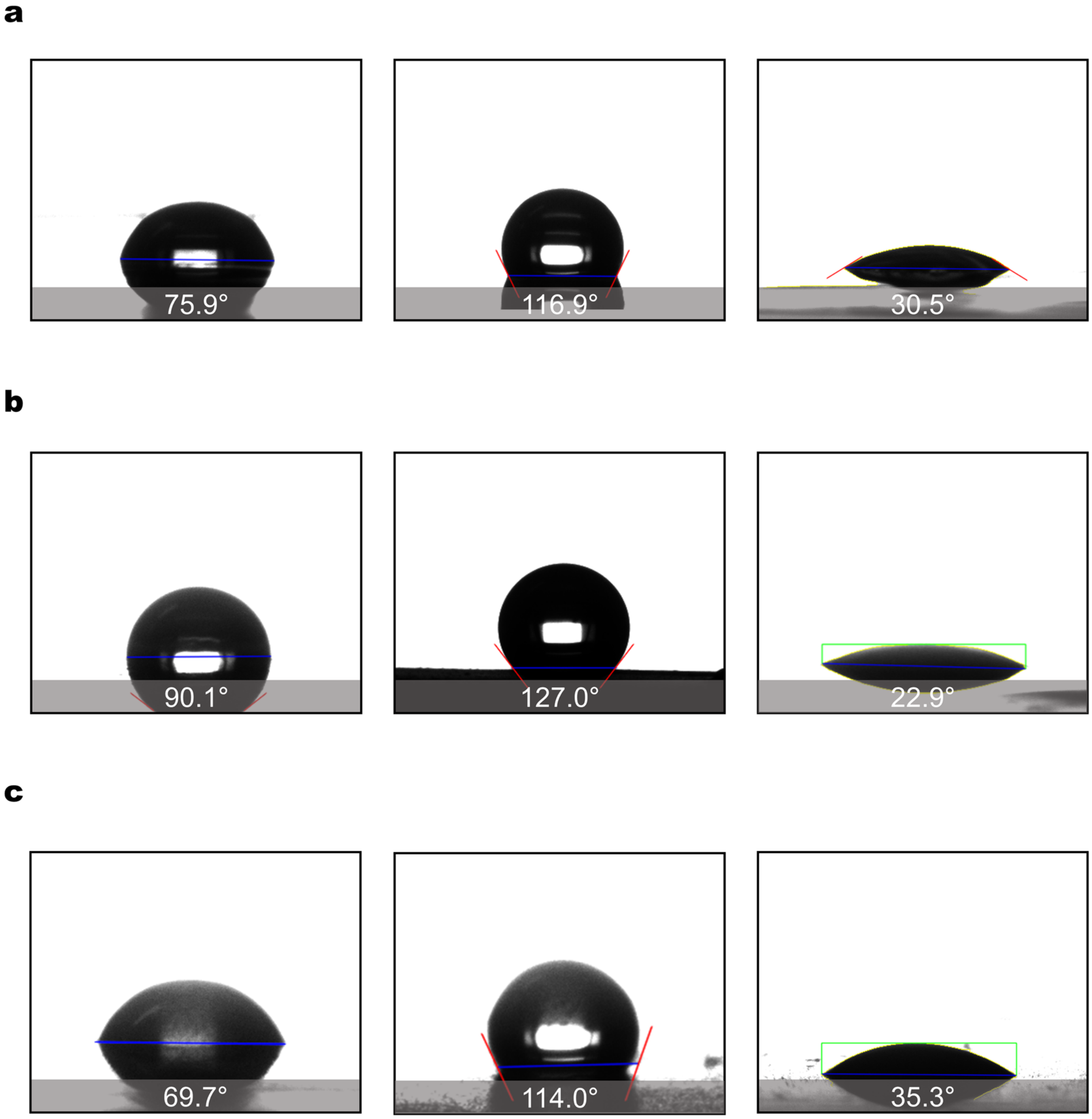

Extended Data Fig. 2 | Material characterization of surface functionalized bioresorbable polymers. a-c Contact angle of (**a**) PLA, (**b**) PHBV, and (**c**) PCL according to surface functionalization. (left: Bare, center: FOTS, right: poly-$_L$-lysine) Decreased contact angles denote improved hydrophilicity, while increased angles indicate enhanced hydrophobicity. Therefore, we confirmed the changes in hydrophilic and hydrophobic properties based on the surface functional groups.

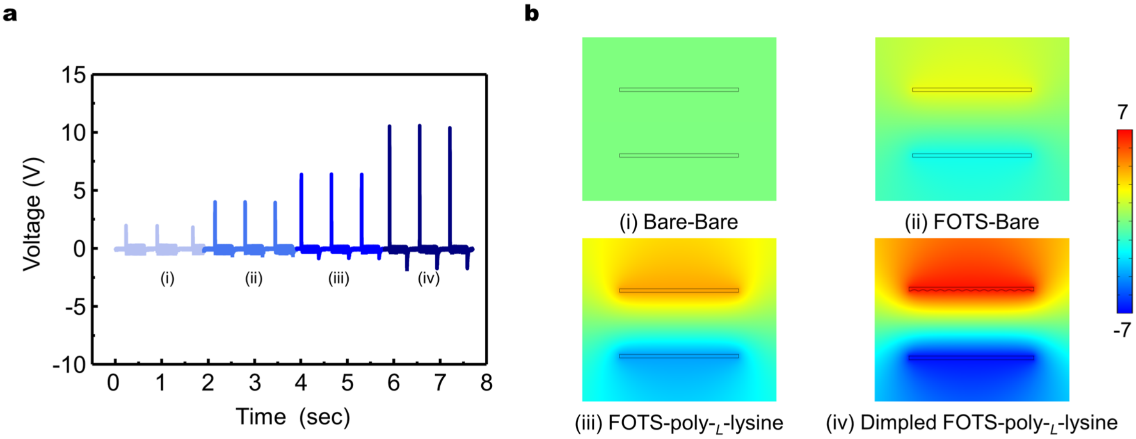

Extended Data Fig. 3 | Triboelectric behavior of surface functionalized/dimple-structured PLGA. a Evaluation of triboelectric voltage output. **b** Comparative analysis of electric potential according to surface functionalization using FEM simulation. (i) Bare-Bare. (ii) FOTS-Bare. (iii) FOTS-poly-$_L$-lysine. (iv) FOTS with dimple structure-poly-$_L$-lysine.

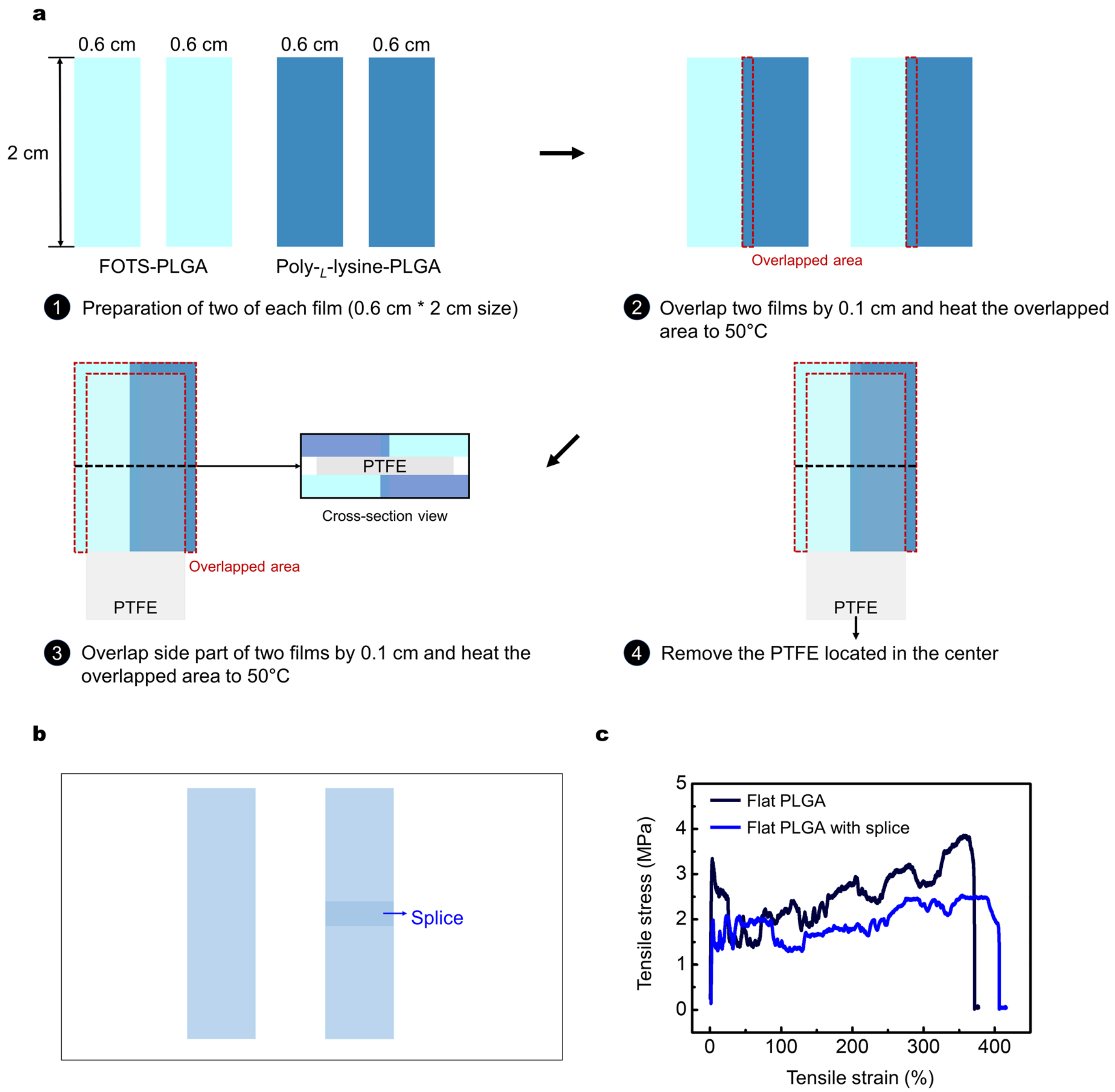

Extended Data Fig. 4 | Encapsulation process of NBAT. a Fabrication process of NBAT. To achieve maximizing triboelectric potential, we physically connect tribopositive and tribonegative layer by heating. **b** Schematic of splice region in PLGA. **c** Comparative analysis of mechanical property in Flat PLGA w/o and w/ splice region. It was confirmed that splice region does not affect the mechanical properties.

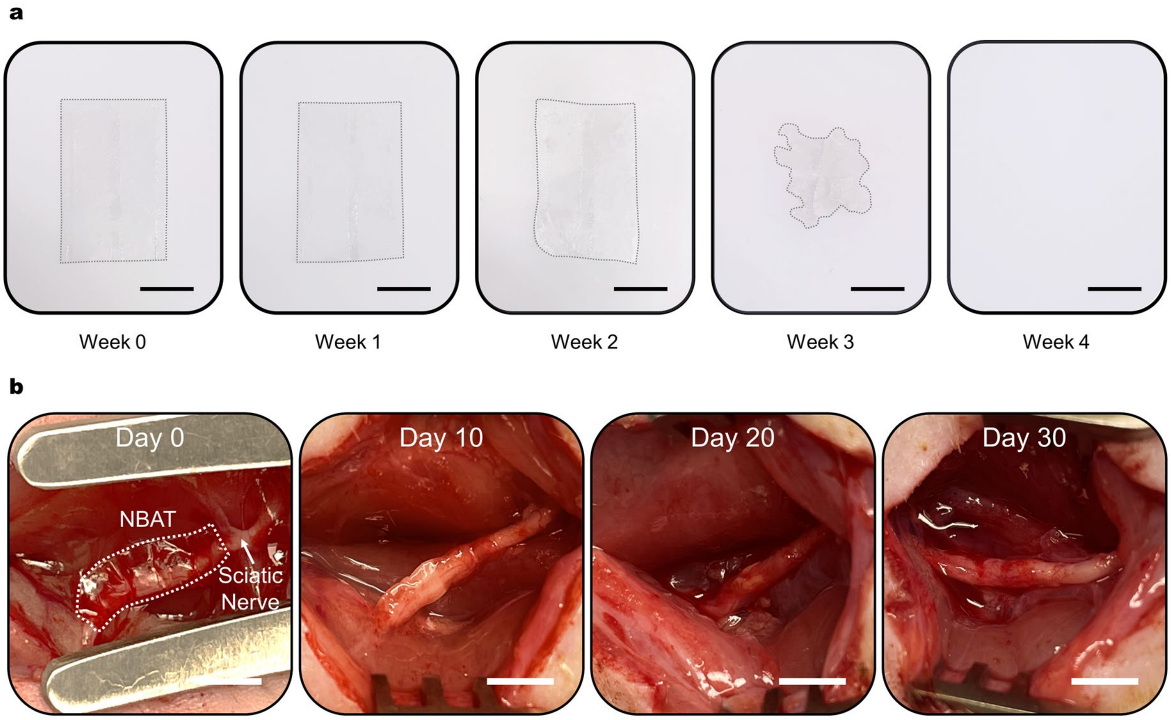

Extended Data Fig. 5 | Transient performance of NBAT. a, b Images of degradation of a NBAT associated with (**a**) immersion in PBS(pH =7.4) at 37 °C and (**b**) implantation in rat. Scale bar, 0.5 cm.

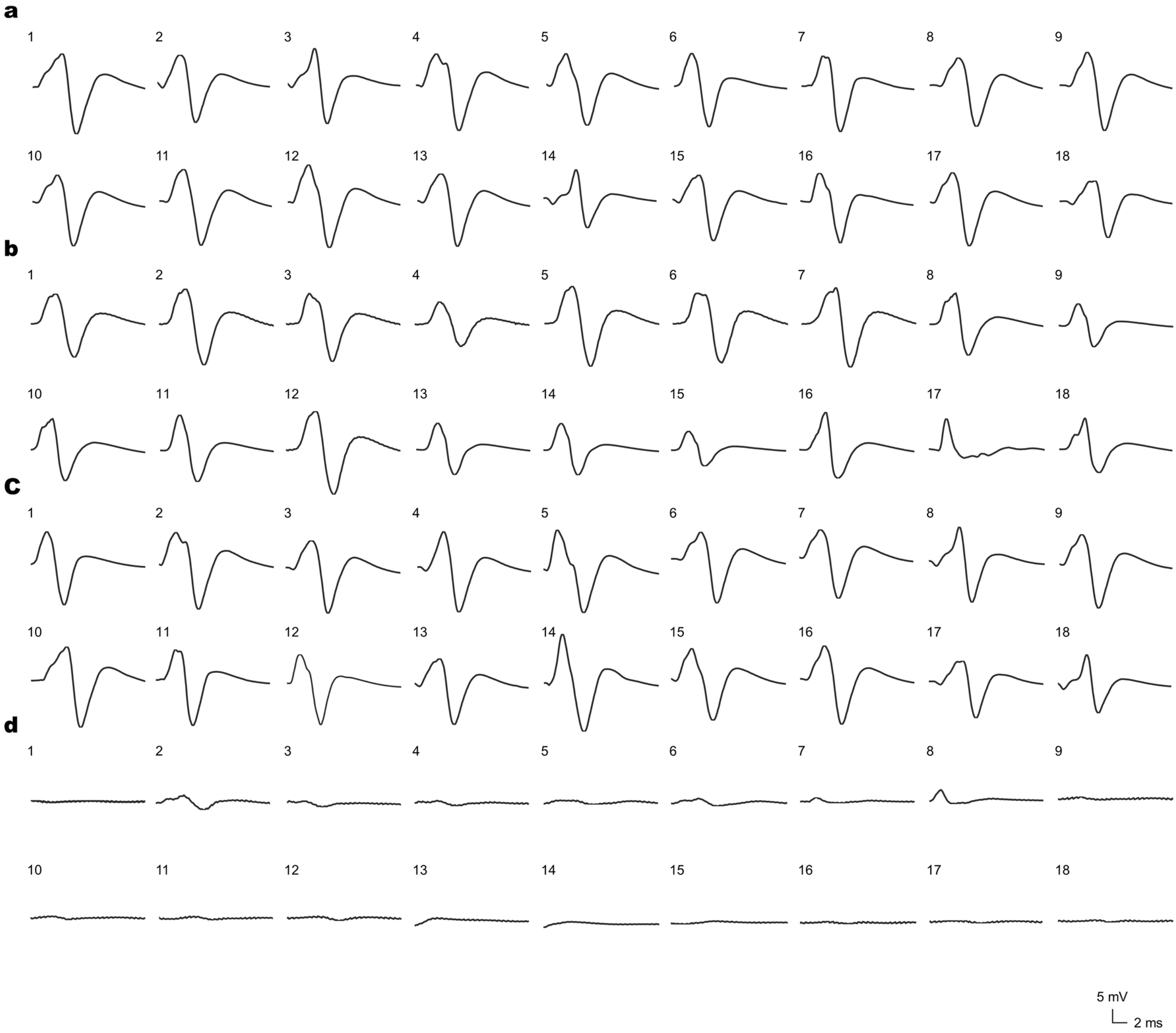

Extended Data Fig. 6 | Line graphs of compound muscle action potential. **a** Control. **b** US. **c** Sham. **d** NBAT.

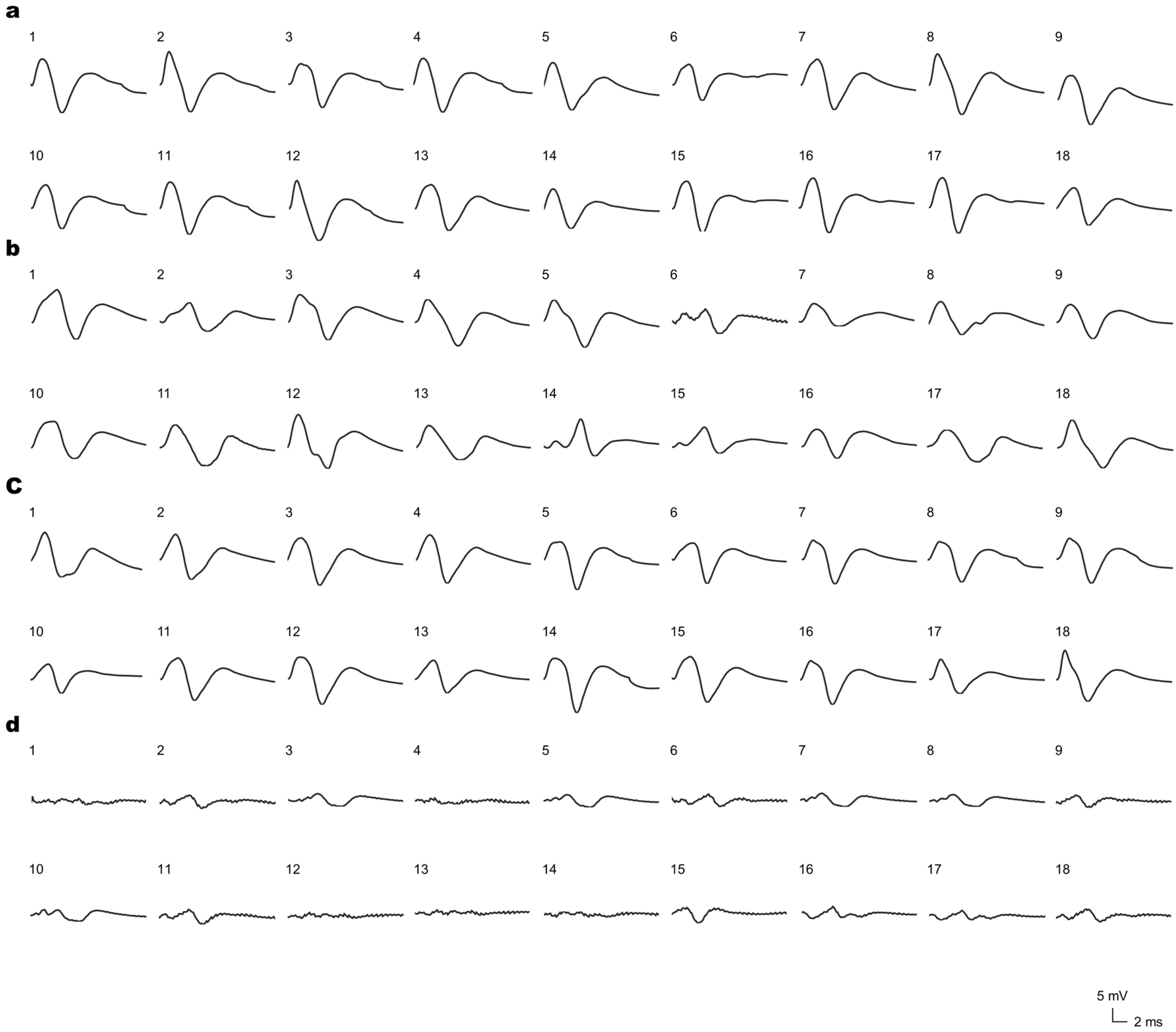

Extended Data Fig. 7 | Line graphs of compound nerve action potential. **a** Control. **b** US. **c** Sham. **d** NBAT.

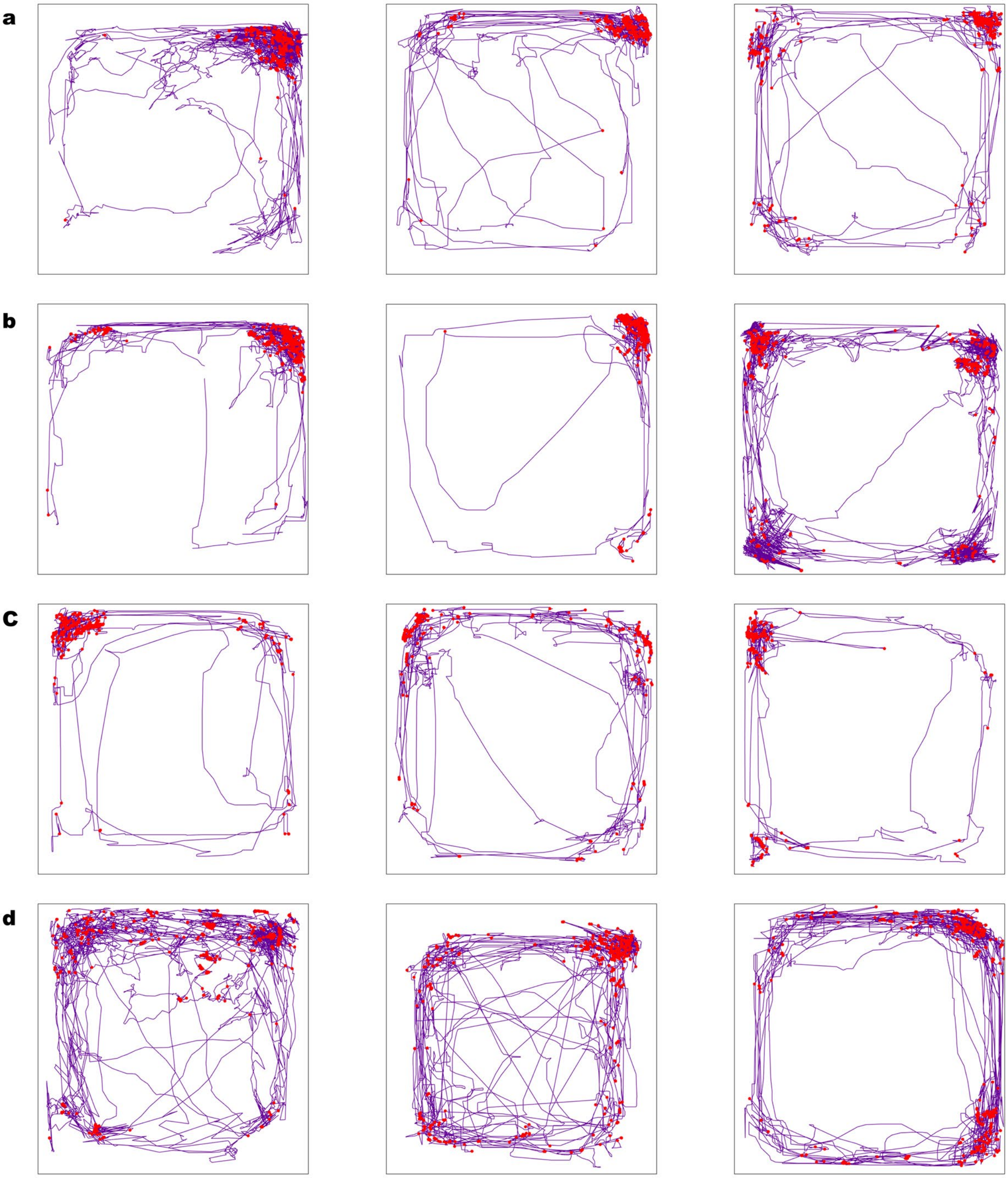

Extended Data Fig. 8 | Representative trajectory plots from open-field behavioral analysis. a Control. **b** US. **c** Sham. **d** NBAT.

nature research

Corresponding author(s): Kyu Hyoung Lee, Byung-Ok Choi, Sang-Woo Kim

Last updated by author(s): Aug 24, 2025

Reporting Summary

Nature Research wishes to improve the reproducibility of the work that we publish. This form provides structure for consistency and transparency in reporting. For further information on Nature Research policies, see our Editorial Policies and the Editorial Policy Checklist.

Statistics

For all statistical analyses, confirm that the following items are present in the figure legend, table legend, main text, or Methods section.

n/a	Confirmed	
☐	☒	The exact sample size (*n*) for each experimental group/condition, given as a discrete number and unit of measurement
☐	☒	A statement on whether measurements were taken from distinct samples or whether the same sample was measured repeatedly
☐	☒	The statistical test(s) used AND whether they are one- or two-sided *Only common tests should be described solely by name; describe more complex techniques in the Methods section.*
☒	☐	A description of all covariates tested
☒	☐	A description of any assumptions or corrections, such as tests of normality and adjustment for multiple comparisons
☐	☒	A full description of the statistical parameters including central tendency (e.g. means) or other basic estimates (e.g. regression coefficient) AND variation (e.g. standard deviation) or associated estimates of uncertainty (e.g. confidence intervals)
☐	☒	For null hypothesis testing, the test statistic (e.g. *F*, *t*, *r*) with confidence intervals, effect sizes, degrees of freedom and *P* value noted *Give P values as exact values whenever suitable.*
☒	☐	For Bayesian analysis, information on the choice of priors and Markov chain Monte Carlo settings
☒	☐	For hierarchical and complex designs, identification of the appropriate level for tests and full reporting of outcomes
☒	☐	Estimates of effect sizes (e.g. Cohen's *d*, Pearson's *r*), indicating how they were calculated

Our web collection on statistics for biologists contains articles on many of the points above.

Software and code

Policy information about availability of computer code

Data collection	Electrical characterization data and neuro signal were collected by digital phosphor oscilloscope (Tektronix, DPO 3052 Digital Phosphor). The action potential of rat was collected by a Nicolet VikingQuest device (Natus Medical).
Data analysis	Electrical characterization data were analyzed using OriginPro 9.0 and Microsoft Excel (Version 16.71, 23031200). Material characterization data were analyzed using OriginPro 9.0 and Microsoft Excel (Version16.71, 23031200). FEM simulations performed in this work were carried out using COMSOL Multiphysics (Version 5.5). All the statistical analysis were conducted using Prism 9 software (Version 9.5.0, GraphPad). Video-based behavioral analysis was performed using custom scripts implemented in MATLAB R2024a to extract movement trajectories, calculate locomotion speed and distance, and visualize motion paths.

For manuscripts utilizing custom algorithms or software that are central to the research but not yet described in published literature, software must be made available to editors and reviewers. We strongly encourage code deposition in a community repository (e.g. GitHub). See the Nature Research guidelines for submitting code & software for further information.

Data

Policy information about availability of data

All manuscripts must include a data availability statement. This statement should provide the following information, where applicable:

- Accession codes, unique identifiers, or web links for publicly available datasets
- A list of figures that have associated raw data
- A description of any restrictions on data availability

The authors that all data supporting the findings of this study are available within the paper and its Supplementary Information. The raw and analysed datasets generated during the study are available from the corresponding authors on request.

Field-specific reporting

Please select the one below that is the best fit for your research. If you are not sure, read the appropriate sections before making your selection.

☒ Life sciences ☐ Behavioural & social sciences ☐ Ecological, evolutionary & environmental sciences

For a reference copy of the document with all sections, see nature.com/documents/nr-reporting-summary-flat.pdf

Life sciences study design

All studies must disclose on these points even when the disclosure is negative.

Sample size	The number of animals was chosen enough to perform statistical analysis.
Data exclusions	No data were excluded.
Replication	All key experiments were independently replicated at least three times with consistent outcomes.
Randomization	The experimental subjects were selected at random
Blinding	Blinding was not required for this study.

Reporting for specific materials, systems and methods

We require information from authors about some types of materials, experimental systems and methods used in many studies. Here, indicate whether each material, system or method listed is relevant to your study. If you are not sure if a list item applies to your research, read the appropriate section before selecting a response.

Materials & experimental systems

n/a	Involved in the study	
☒	☐	Antibodies
☐	☒	Eukaryotic cell lines
☒	☐	Palaeontology and archaeology
☐	☒	Animals and other organisms
☒	☐	Human research participants
☒	☐	Clinical data
☒	☐	Dual use research of concern

Methods

n/a	Involved in the study	
☒	☐	ChIP-seq
☒	☐	Flow cytometry
☒	☐	MRI-based neuroimaging

Eukaryotic cell lines

Policy information about cell lines

Cell line source(s)	Human fibroblasts (ATCC, CRL-1502) were used in this study (Designation: WS1; Product category: Human cells; Organism: Homo sapience, human; Cell type: Fibroblast; Morphology: Fibroblast).
Authentication	The human fibroblasts purchased through ATCC were not authenticated
Mycoplasma contamination	The human fibroblasts (ATCC, CRL-1502) were tested negative for mycoplasma contamination.
Commonly misidentified lines (See ICLAC register)	No commonly misidentified cell lines were used in this work.

Animals and other organisms

Policy information about studies involving animals; ARRIVE guidelines recommended for reporting animal research

Laboratory animals	Animal experiments were performed using healthy adult Sprague-Dawley rats (8-9 weeks, female, 250-320 g) and crossbred pigs (Sus scrofa domesticus; Landrace × Yorkshire × Duroc, LYD) (10 weeks old, male, 30 ± 2 kg) were obtained from XPbio Inc. (Korea).
Wild animals	The study did not involve wild animals.
Field-collected samples	The study did not involve samples collected from the field.
Ethics oversight	All procedures involving implantation, electrical stimulation, and biosignal monitoring of the experimental subjects were performed

Ethics oversight	in accordance with appropriate protocols. Rat-based study was reviewed and approved by the Institutional Animal Care and Use Committee (IACUC) of Samsung Medical Center (20240109001). Subsequently, large animal study using pig was reviewed and approved by IACUC of BIOSTEP (23-KE-0493).

Note that full information on the approval of the study protocol must also be provided in the manuscript.